Composites Science and Technology 104 (2014) 34–39

Contents lists available at ScienceDirect

Composites Science and Technology

journal homepage: www.elsevier.com/locate/compscitech

Quantitative mapping of mechanical properties in polylactic acid/natural rubber/organoclay bionanocomposites as revealed by nanoindentation with atomic force microscopy

D.E. Martínez-Tong [a,*], A.S. Najar [b], M. Soccio [a,1], A. Nogales [a], N. Bitinis [b], M.A. López-Manchado [b], T.A. Ezquerra [a,*]

[a] Instituto de Estructura de la Materia, IEM-CSIC, Serrano 121, 28006 Madrid, Spain
[b] Instituto de Ciencia y Tecnología de Polímeros, ICTP-CSIC, Juan de la Cierva 3, 28006 Madrid, Spain

ARTICLE INFO

Article history:
Received 26 March 2014
Received in revised form 28 August 2014
Accepted 31 August 2014
Available online 6 September 2014

Keywords:
A. Particle-reinforced composites
A. Nano composites
B. Mechanical Properties
D. Atomic Force Microscopy (AFM)

ABSTRACT

Quantitative mapping of the mechanical properties of a series of polylactic acid/natural rubber/organoclay bionanocomposites has been accomplished by using nanoindentation with atomic force microscopy. Topography, elastic modulus and adhesion maps were obtained simultaneously revealing nanoscopic mechanical features in the samples associated to the different phases. For polylactic acid and polylactic acid/natural rubber a single distribution of Young's moduli was obtained whose maximum correlates well with the macroscopic measurements. Bionanocomposites with high organoclay loads exhibit a bimodal distribution of elastic moduli whose maxima can be associated to the polylactic acid matrix and to the reinforcing levels provided by the organoclay component. Adhesion maps allow one to obtain mechanical contrast between polylactic acid and organoclay, at high loadings, revealing the good compatibility of the organoclay with the polymer.

1. Introduction

Bionanocomposites are a class of hybrid materials formed by the combination of a biopolymer and nanoadditives [1]. The development of these materials is mainly driven by the attempt to couple intrinsic natural polymer properties such as biocompatibility and biodegradability with enhanced mechanical and thermal stability. Polylactic acid (PLA) is a linear aliphatic polyester being both biodegradable and biocompatible. Although useful for a broad range of medical procedures [2–4] its mechanical properties are weak since it bears only small deformations before mechanical fracture [5]. One possibility to overcome this problem is by blending intrinsically brittle PLA with natural rubber (NR) aiming to improve its toughness [6]. Being PLA and NR intrinsically not compatible, it has been demonstrated that organoclays can act as effective compatibilizers through their preferential location at the polymer interfaces, reducing the interfacial tension and preventing the coalescence of the dispersed phase [5–7]. In general, performance of these blends strongly depends on the microscopic morphology which in turn determines the micromechanical deformation mechanisms [8,9]. Indentation with an Atomic Force Microscope (AFM) is a versatile method especially suited to study local mechanical properties of materials [10–14]. AFM provides not only information on the surface morphology of polymer materials but also a complete battery of physical properties including electrical [15], mechanical [11,16,17], dielectrical [18,19] and piezoelectrical [20,21] among others. As far as the mechanical properties are concerned, it is still a challenging problem the quantitative evaluation and the comparison with the macroscopic values [11]. Although quantitative nanomechanical reports on PLA [16] and synthetic rubber [17] have been published, according our knowledge no similar studies on PLA/NR/organoclay bionanocomposites have been reported. Until now, most of the mechanical studies performed on these types of ternary blends have been accomplished by macroscopic stress–strain and concurrent analysis of fractured surfaces either by microscopy [22,23] or by X-ray scattering methods [24].

Here we present a quantitative investigation on the mechanical properties of a series of PLA/NR/organoclay bionanocomposites with the main aim of obtaining information at the nanoscale, where the length scales are relevant for the understanding of deformation and eventual rupture of these materials.

* Corresponding authors.
E-mail addresses: d.martinez@iem.cfmac.csic.es (D.E. Martínez-Tong), t.ezquerra@csic.es (T.A. Ezquerra).
[1] Present address: Dipartimento di Ingegneria Civile, Chimica, Ambientale e dei Materiali, Universitá di Bologna, via Terracini 28, 40131 Bologna, Italy.

http://dx.doi.org/10.1016/j.compscitech.2014.08.030
0266-3538/

2. Experimental part

2.1. Materials

Polylactic acid (PLA) was provided by NatureWorks®. The selected grade, PLA 2002D (D-content 4.25%, ρ = 1.24 g/cm^3), is a semicrystalline extrusion material with a residual monomer content of 0.3%. Natural rubber (NR) was kindly supplied by Malaysian Rubber under the trade name CV60 (Mooney viscosity ML (1 + 4) 100 °C = 60). Two organo-modified montmorrillonites, denoted as Cloisite 15A (C15A) and Cloisite 30B (C30B) were purchased from Southern Clays Products and used as fillers. C15A is modified with dimethyl dehydrogenated tallow alkyl ammonium cation. The presence of this surfactant has proven to improve the affinity between this organoclay and NR phases [6]. C30B is modified with bis(2-hydroxyethyl)-methyl tallow alkyl ammonium cation, which when blended with PLA and NR, usually locates in the PLA matrix [6]. PLA and clays were dried overnight in a desiccating dryer at 80 °C prior to use. The bionanocomposites were prepared by melt blending in a Haake Minilab twin screw extruder following the optimal processing conditions previously reported [6]. The NR concentration in the blend was fixed at 10 wt%, and the organoclay loadings were 1 and 5 wt%, as shown in Table 1.

2.2. Atomic Force Microscopy (AFM) nanoindentation measurements

AFM measurements were carried out in a Bruker Multimode 8, with a Nanoscope V controller, by the PeakForce Quantitative Nanomechanical Mapping (PF-QNM) method. All measurements were made under ambient conditions at room temperature, using a standard cantilever holder. Measurements were performed over randomly selected surface areas, at a resolution of 512 × 512 pixels. Mechanical properties of the cantilever, as well as tip geometry must be taken into consideration when performing PF-QNM measurements in order to get the best possible outcome. All quantitative measurements were carried out with MPP-2110–10 probes (Bruker). The actual cantilever spring constant (k, nominally 1–6 N/m), was measured by the thermal tune method and found to be around 2–3 N/m. Tip radius was calibrated against a polystyrene standard provided by Bruker. The measured value of the tip radius was 10 nm. PF-QNM is a contact AFM protocol, based on the force-volume method. In these types of methods, force-distance curves are collected by nanoindentation of the sample in a point-by-point fashion. The maximum force (peak force) is controlled at each pixel to obtain force-distance curves which are then used as feedback signal. In this method, the piezo-scanner is oscillated at 2 kHz, while the probe remains at rest, which allows a high speed and simultaneous capture of force-distance curves with topography images. This feature is the main advantage of PF-QNM over the classical nanoindentation methods and previous AFM protocols for measuring mechanical properties [25,26].

Fig. 1a shows a PF-QNM height image of a PLA-NR bionanocomposite. The droplet like dark area corresponds to NR sites inside the PLA matrix, as evidenced in previous works [1,5]. Fig. 1b and c shows two examples of the PF-QNM force-distance curves, collected in the PLA matrix region and in the NR droplet at a constant

Table 1
Composition of the bionanocomposites investigated.

Sample	NR (wt%)	C15A (wt%)	C30B (wt%)
PLA	0	0	
PLA-NR	10		
C15A-1		1	0
C15A-5		5	0
C30B-1		0	1
C30B-5		0	5

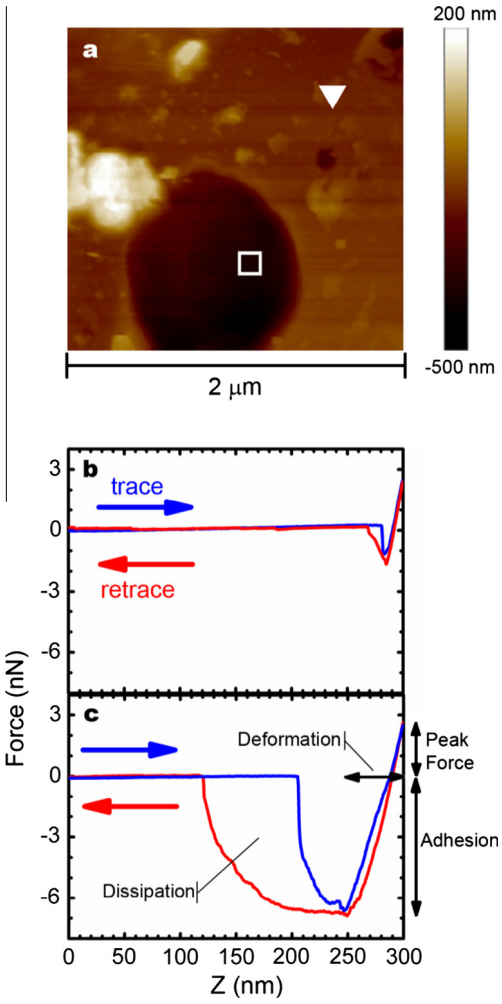

Fig. 1. (a) PF-QNM topography image of a PLA-NR bionanocomposite. (b) Force-distance (Z) curves in the PLA region (▽) and (c) in the NR droplet (□) while approaching the sample surface (trace, blue line) and withdrawal (retrace, red line). (For interpretation of the references to colour in this figure legend, the reader is referred to the web version of this article.)

ramp rate of 0.5 Hz. In Fig. 1 (bottom), the Z-axis reflects the distance ramped by the piezo-scanner in the vertical direction. Upon approaching (trace) the tip to the sample an initial attractive force appears. This is followed by an elastic regime in which the force is proportional to the deformation. Upon withdrawal (retrace), the adhesion force is related to the minimum in the force–distance curve. The difference between the area covered by the force–distance curve in the approaching and withdrawal process is defined as dissipation. The experimental conditions were chosen in order to study the nanomechanical response of each of the components of the bionanocomposites in the elastic regime. Analysis of the force-curves is automatically performed by the equipment and the topography, elastic modulus, adhesion force, deformation and dissipation can be simultaneously measured by the system. To obtain the Young's Modulus, the retrace curve is fitted by the software using the Derjaguin–Muller–Toporov (DMT) model [27]:

$$F - F_{adh} = \frac{4}{3}E^* \sqrt{R(d - d_0)^3} \quad (1)$$

where F–F_{adh} is the force on the cantilever (F) relative to the adhesion force (F_{adh}), R is the tip end radius, and $d - d_0$ is the deformation of the sample, *i.e.* penetration of the tip in the sample. The result of the fit is the reduced modulus E^*. The Young's Modulus of the sample (E_{YOUNG}) can be calculated with the following equation:

$$E^* = \left[\frac{1-\upsilon_s^2}{E_{YOUNG}} + \frac{1-\upsilon_{tip}^2}{E_{tip}}\right]^{-1} \quad (2)$$

where υ_s is the Poisson's ratio of the sample, υ_{tip} the Poisson's ratio of the tip and E_{tip} the mechanical modulus of the tip. If one assumes that the modulus of the tip is very high in comparison to that of the sample then the second term in the right hand side of Eq. (2) can be neglected in a first approach. In this case, the Young's Modulus only depends on the υ_s value. In this work, the reduced modulus data were transformed into Young's modulus following Eq. (2) and taking a value of $\upsilon_s = 0.35$ for PLA [28,29] and $\upsilon_s = 0.5$ for Natural Rubber [30–32] as previously reported in the literature.

2.3. Surface preparation

In this work, two approaches for sample preparation were explored following the ideas previously developed for electron microscopy studies of these bionanocomposites [6]. In the first case, the PLA sample was cryo-fractured in liquid nitrogen, while in the second one, the top face of a 1 mm thick PLA sample was sectioned with a Leica EM UC6 cryo-ultramicrotome at −140 °C. Fig. 2 shows PF-QNM topography images with the corresponding height profiles of both approaches. For each method, a scan area of 5 × 5 μm is presented.

Fig. 2a shows the topography image of a PLA sample cryo-fractured in liquid nitrogen. Its height section cut shows a strong rugosity of about ±100 nm. Fig. 2c shows the topography image of a sample sectioned with a Leica EM UC6 cryo-ultramicrotome. Height section cut shows that the rugosity decreased by a factor 10 under this cutting method. At the same time, the fact that sample thickness is as high as 1 mm avoids the probe interaction with the sample holder, which accounts for substrate effects on the mechanical measurements [33]. After comparison between these results, all samples for mechanical measurements were prepared by cryo-ultramicrotomy.

3. Results and discussion

3.1. Nanomechanical properties

Fig. 3 shows the results for four selected samples. PF-QNM images of topography, elastic modulus and adhesion force are presented with their corresponding profiles, along the dashed line of distance *x*.

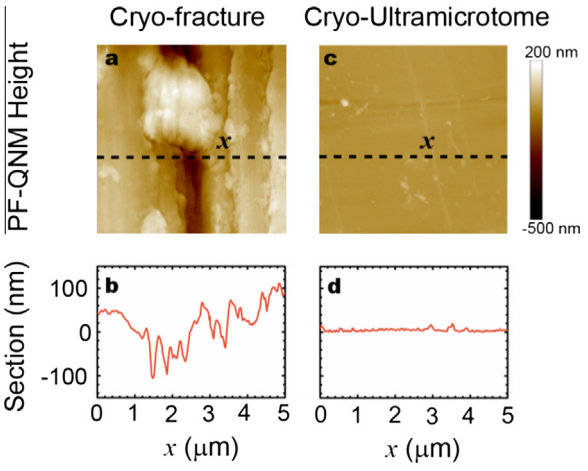

Fig. 2. PF-QNM topography of (a) cryo-fracture and (c) cryo-ultramicrotome cut of a PLA sample. (b and d) surface profile along the lines *x*. AFM images are 5 × 5 μm squares.

First top row of Fig. 3 shows the PF-QNM height images. PLA shows a flat topography, with roughness of about 10 nm. Some height features are present, randomly distributed through the image consequence of the cryo-ultramicrotomy cut. The mixture of PLA with NR (PLA-NR) is characterized by the presence of NR droplets like motives over the whole topography image. These droplets exhibit an almost circular shape with diameters ranging from 50 to 1000 nm and depths in the order of 300 nm as evidenced in its height profile (second row). It is worth mentioning that the use of samples with thicknesses larger than the depths of the NR droplet is a requirement in this case. For this reason, we have not performed regular ultramicrotomy cuts, generally used for transmission electron microscopy, since they provide samples with thicknesses below 100 nm. The introduction of the organoclays within the PLA-NR system affects the shape of the NR droplets. For the nanocomposite with 5 wt% of the C15A, elongated/agglomerated NR regions can be seen in the topography image. In this case, the NR regions seem to be formed by the coalescence of individual droplets, as evidenced from the height profile. The depth of the coalesced NR droplets is smaller in comparison to the PLA-NR blend. For the nanocomposite with 5 wt% of the C30B a decrease of the droplet sizes in comparison to those of the PLA-NR system is also evidenced. In addition, the depth of the droplets also decreases. As discussed by Bitinis et al. [6], the decrease of size of the NR droplets is mainly related to two effects. First, the compatibility of the clay with the PLA and NR phases and second, the change of the viscosity ratio of the blend phases as the organoclay is added. The presence of C30B organoclay in the PLA phase increases its viscosity and facilitates the droplet breakup of the dispersed high viscosity rubber phase, inducing a further decrease of the droplet size [6]. Third and fourth row from the top in Fig. 3 show the PF-QNM images of the elastic modulus and their section profile along *x*, respectively. Following the analysis presented above, these elastic modulus images represent a map of the Young's modulus (E_{YOUNG}) of the sample. In the PLA case, a constant elastic modulus is found along the whole image. The image profile shows that the Young's modulus varies around 2–3 GPa. Since the sample is not completely flat, different areas present slight distinct probe-sample interaction, causing this variation [25]. The value of Young's modulus remains similar in the PLA matrix of the PLA-NR sample. However, inside the droplets, the elastic modulus decreases dramatically. This corroborates the presence of NR inside the droplet like regions. Blends with organoclays show an increase of the Young's modulus in the matrix for both C15A-5 and C30B-5, as seen in the profiles images. The bionanocomposite C15A-5 also shows a decrease of elastic modulus inside the droplets, revealing the presence of NR. However, C30B-5 shows no elastic modulus variation, between matrix and droplets. This suggests that in C30B-5, due to the increasing toughness of the matrix, the NR could be partially dragged by the ultramicrotomy blade. The Young's modulus of the bionanocomposite matrices were evaluated by excluding the NR regions of the AFM images. For several images of all samples different square areas of the matrix were selected with sizes of varying between 100 to 1000 nm. These limits were chosen in order to overcome noise from probe-sample interactions (areas below 100 nm) and to avoid the presence of NR droplets (areas above 1000 nm). In each square, the values of the modulus were recorded and plotted in a histogram. Fig. 4 shows the Young's modulus histograms, resulting from this analysis, for four selected samples. Histograms were fitted with Gaussian distributions.

PLA and PLA-NR show a clear maximum around 2.5 GPa, as expected from elastic modulus profiles in Fig. 3. Distribution of higher modulus values in the PLA-NR sample, between 4 and 5 GPa, are related to probe-sample interactions in high rugosity areas which could not be avoided. Also, elastic modulus of the

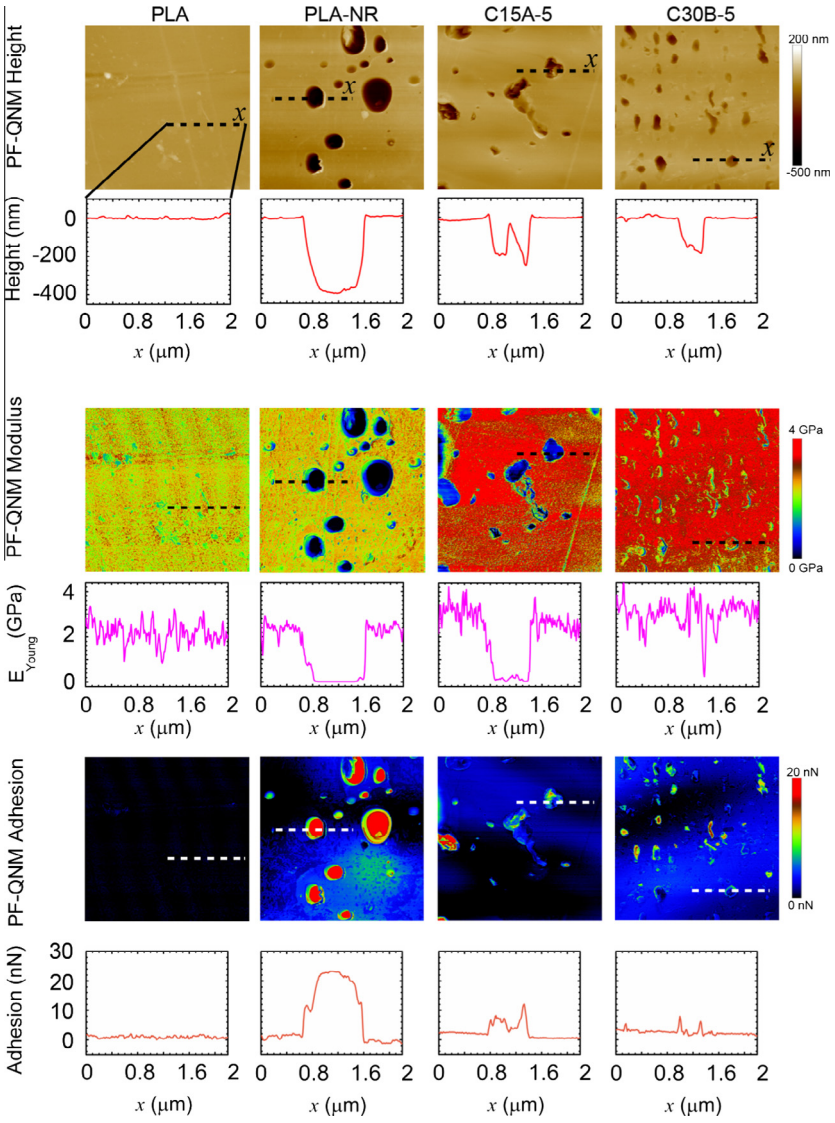

Fig. 3. PF-QNM images for the investigated samples. From top to bottom, topography, elastic modulus and adhesion force presented with their corresponding profiles, along the line *x* indicated in the corresponding image. AFM images are 5 × 5 μm squares.

NR droplets were quantified in the PLA-NR samples, where a mean value of 12 MPa was found.

Organoclay reinforced samples show a bi-modal distribution of the Young's modulus in their matrices. In both cases, a first peak around 2 GPa can be related to the modulus of the PLA while the second peak, around 3 GPa, can be related to the reinforced zones. For the C30B organoclay loading, this distribution of Young's modulus can be interpreted straight forward from the affinity between matrix and organoclay loading. Nevertheless, as stated previously, it is expected that the C15A organoclay shows affinity with the NR phase and thus, reinforcement should not necessarily be expected in the PLA matrix. However, there could be reinforced NR sites just below the PLA matrix surface that although nor directly visualized in the PF-QNM topography image could contribute to the mechanical response as evidenced by the bi-modal distribution measured in the Young's modulus. Fig. 5 shows the values of E_{YOUNG} as estimated by the PF-QNM method for all the samples (red bars). The value of the Young's modulus was taken from the fitted value of peak maxima in the Gaussian distributions. The error bars are related to the uncertainty of this fitting parameter.

One observes a Young's modulus around 2.4 ± 0.2 GPa for the PLA matrix. This value slightly decreased by adding 1 wt% of organoclay. Only at high organoclay loadings (5 wt%) the bimodal distribution appears and an overall reinforcement of the matrix of about 1 GPa is found. In Fig. 5, the blue bars are the Young's modulus values for these samples estimated by standard macroscopic strain–stress tests on an Instron dynamometer as previously reported [6]. In principle the relationship between the macroscopic elastic modulus and the AFM based elastic modulus should be related to the volume fraction of the NR particle since by AFM we are estimating images excluding the NR regions. However, overall good agreement between PF-QNM and macroscopic measurements is found, which can be related to the macroscopic nature of the sample used for AFM (thickness about 1 mm). As the tip probes the continuous surface, the organoclay surface distribution can be related to the increase of the Young's modulus values observed for samples C15A-5 and C30B-5, as previously evidenced for nanomechanical measurements of polymer composites [33,34]. Also, one might expect that the properties of NR droplets and organoclay particles underneath might contribute to the nanomechanical measurement, just like substrate influence affects these type of measurements when performed in thin films [33]. Interestingly enough, for the C30B-5 sample the macroscopic value corresponds to the average between the two ones found by the

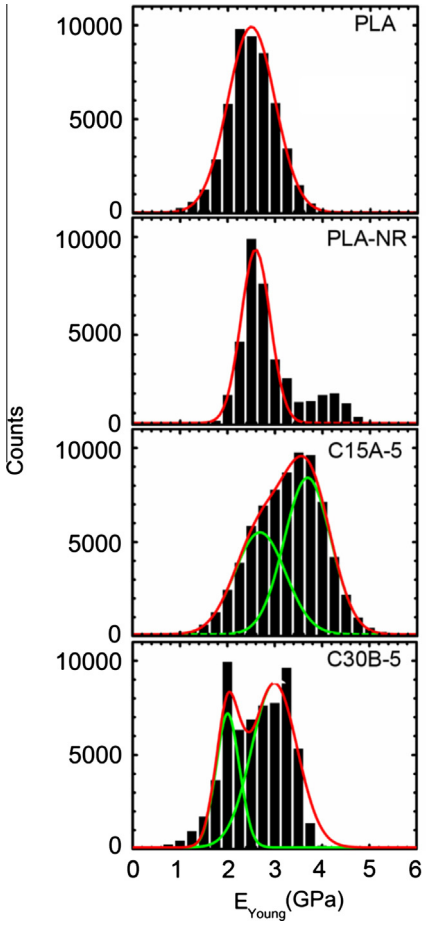

Fig. 4. Young's modulus histograms for (from top-to-bottom): PLA, PLA-NR, C15A-5, C30B-5.

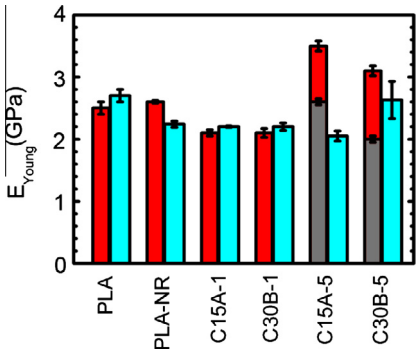

Fig. 5. (Red) PF-QNM Young's modulus values for PLA-NR-Organoclay bionanocomposites. (Blue) Young's modulus evaluated via an Instron dynamometer [6]. For the C15A-5% and C330B-5% samples the gray bar indicate the first maximum of the bimodal distribution (Fig. 4). (For interpretation of the references to colour in this figure legend, the reader is referred to the web version of this article.)

nanometric PF-QNM analysis. This suggests that PF-QNM evidences structural heterogeneities associated to PLA regions with different local nanoclay concentration, not detectable by macroscopic measurements.

3.2. Organoclay distribution

As mentioned before, rows 5 and 6 from the top in Fig. 3 show the PF-QNM adhesion force images and the corresponding profiles along a given length *x*. In all cases, the matrix shows an almost

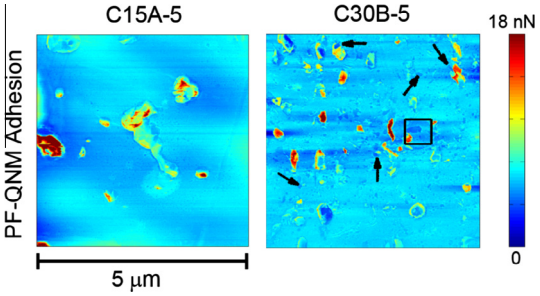

Fig. 6. PF-QNM adhesion images for the samples with higher organoclay content (C15A-5 and C30B-5). Arrows in C30B-5 indicate randomly distributed zones with low adhesion.

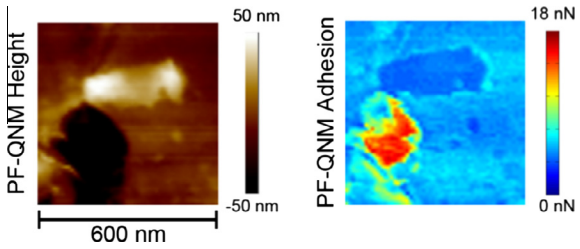

Fig. 7. Magnification of square region marked in Fig. 6-right of the C30B-5 sample. (Left) PF-QNM height image. (Right) PF-QNM adhesion image.

constant adhesion value close to zero. However, in the droplet like NR phase an increase is observed. This can be attributed to the higher viscosity of NR (glass transition temperature $T_g = -73$ °C) in comparison to that of PLA ($T_g = 58$ °C). By addition of both organoclays, the adhesion of the blend is clearly decreased. In order to further exploit the performance of PF-QNM measurements, we have analyzed in higher detail the adhesion images with the aim of gaining information about the organoclay dispersion in the bionanocomposites. Fig. 6 shows the PF-QNM adhesion images for the samples with higher organoclay content (C15A-5 and C30B-5). While C15A-5 exhibits constant adhesion values throughout the whole matrix, the C30B-5 sample shows some contrast in the adhesion features of the matrix indicated by arrows in the image. These motives are randomly distributed and present lower adhesion values than those of the matrix. On the C30B-5 image, Fig. 6, a square region is chosen to further analyze the mechanical behavior of the adhesion features, and is presented in Fig. 7.

Fig. 7 shows an area of the C30B-5 sample, where an adhesion feature was detected. Here, the PF-QNM height and adhesion image show that this feature corresponds to a plateau of about 40 nm thick. The height image shows that this feature corresponds to a plateau of about 40 nm thick. The adhesion map shows that throughout the whole plateau, the value of the adhesion reduces to values lower than those of the matrix. These facts, along with the known compatibility of the C30B organoclay with PLA [6], lead to identify these adhesion features with the organoclay phase dispersed throughout the matrix.

4. Conclusions

PF-QNM measurements were carried out in PLA-NR-Organoclay bionanocomposites. Topography, elastic modulus and adhesion maps were obtained simultaneously. Values of the Young's modulus for the different matrices were obtained from the elastic modulus maps. For PLA, PLA-NR and the nanocomposites with low loads of organoclays (1 wt%), a single distribution of Young's moduli centered around of 2.4 ± 0.2 GPa was obtained. This value

correlates well with the macroscopic measurements. Nanocomposites with high organoclay loads (5 wt%) exhibit a bimodal distribution of elastic modulus. In these cases, the maximum of the lower component has been assigned to the PLA matrix while the higher one has been associated to the reinforced PLA-organoclay. In addition, adhesion maps allowed obtaining mechanical contrast between PLA and C30B organoclay at high nanofiller loads. This effect further supports the compatibility of the C30B organoclay with PLA.

Acknowledgments

The authors gratefully acknowledge the financial support of the *Spanish Ministry of Science and Innovation* (MICINN) through MAT 2010-18749, MAT 2011-23455 and MAT 2012-33517. D.E.M. and M.S. thank CSIC for the tenure of JAE-Pre fellowship and JAE-Doc contract respectively, and Fondo Social Europeo (FSE) for cofinancing the JAE Program.

Appendix A. Supplementary material

Supplementary data associated with this article can be found, in the online version, at http://dx.doi.org/10.1016/j.compscitech.2014.08.030.

References

[1] Bitinis N, Hernandez M, Verdejo R, Kenny JM, Lopez-Manchado MA, Lopez Manchado MA. Recent advances in clay/polymer nanocomposites. Adv Mater 2011;23(44):5229–36.
[2] Sodergard A, Södergård A, Stolt M. Properties of lactic acid based polymers and their correlation with composition. Prog Polym Sci 2002;27(6):1123–63.
[3] Thomson RC, Wake MC, Yaszemski MJ, Mikos AG. Biodegradable polymer scaffolds to regenerate organs. Adv Polym Sci 1995;122:245–74.
[4] Kim H, Bae E, Kwon I, Pal R, Nam J, Lee D. Effect of PEG-PLLA diblock copolymer on macroporous PLLA scaffolds by thermally induced phase separation. Biomaterials 2004;25(12):2319–29.
[5] Bitinis N, Verdejo R, Cassagnau P, Lopez-Manchado MA, Lopez Manchado MA. Structure and properties of polylactide/natural rubber blends. Mater Chem Phys 2011;129(3):823–31.
[6] Bitinis N, Verdejo R, Maya EM, Espuche E, Cassagnau P, Lopez Manchado MA. Physicochemical properties of organoclay filled polylactic acid/natural rubber blend bionanocomposites. Compos Sci Technol 2012;72(2):305–13.
[7] Silva SML, Lopez-Manchado MA, Arroyo M. Thermoplastic olefin/clay nanocomposites. Effect of matrix composition, and organoclay and compatibilizer structure on morphology/properties relationships. J Nanosci Nanotechnol 2007;7(12):4456–64.
[8] Kim GM, Michler GH. Micromechanical deformation processes in toughened and particle-filled semicrystalline polymers: Part 1. Characterization of deformation processes in dependence on phase morphology. Polymer 1998;39(23):5689–97.
[9] Kim GM, Michler GH. Micromechanical deformation processes in toughened and particle filled semicrystalline polymers: Part 2. model representation for micromechanical deformation processes. Polymer 1998;39(23):5699–703.
[10] Schönherr H, Vancso G. Scanning force microscopy of polymers. Heidelberg: Springer; 2010.
[11] Dokukin M, Sokolov I. Quantitative mapping of the elastic modulus of soft materials with HarmoniX and PeakForce QNM AFM modes. Langmuir 2012;28(46):16060–71.
[12] Martín J, Muñoz M, Encinar M, Calleja M, Martín-González M. Fabrication and mechanical characterization of semi-free-standing (conjugated) polymer thin films. Langmuir 2013.
[13] Balani K, Agarwal A. Damping behavior of carbon nanotube reinforced aluminum oxide coatings by nanomechanical dynamic modulus mapping. J Appl Phys 2008;104(6).
[14] Facca S, Lahiri D, Fioretti F, Messadeq N, Mainard D, Benkirane-Jessel N, et al. In vivo osseointegration of nano-designed composite coatings on titanium implants. ACS Nano 2011;5(6):4790–9.
[15] Riedel C, Alegria A, Schwartz GA, Arinero R, Colmenero J, Alegría A, et al. On the use of electrostatic force microscopy as a quantitative subsurface characterization technique: a numerical study. Appl Phys Lett 2011;99(2):023101.
[16] Liu H, Chen N, Fujinami S, Louzguine Luzgin D, Nakajima K, Nishi T. Quantitative nanomechanical investigation on deformation of poly(lactic acid). Macromolecules 2012;45(21):8770–9.
[17] Igarashi T, Fujinami S, Nishi T, Asao N, Nakajima K, Nakajima A. Nanorheological mapping of rubbers by atomic force microscopy. Macromolecules 2013;46(5):1916–22.
[18] Labardi M, Prevosto D, Nguyen K, Capaccioli S, Lucchesi M, Rolla P. Local dielectric spectroscopy of nanocomposite materials interfaces. J Vac Sci Technol B, Microelectron Nanometer Struct Process, Measur Phenomena 2010;28(3):C4D11.
[19] Schwartz GA, Riedel C, Arinero R, Tordjeman P, Alegria A, Colmenero J. Broadband nanodielectric spectroscopy by means of amplitude modulation electrostatic force microscopy (AM-EFM). Ultramicroscopy 2011;111(8):1366–9.
[20] Sharma P, Reece T, Ducharme S, Gruverman A. High-resolution studies of domain switching behavior in nanostructured ferroelectric polymers. Nano Lett 2011;11(5):1970–5.
[21] Martinez-Tong DE, Soccio M, Garcia-Gutierrez MC, Nogales A, Rueda DR, Alayo N, et al. Improving information density in ferroelectric polymer films by using nanoimprinted gratings. Appl Phys Lett 2013;102(19):191601.
[22] Dasari A, Yu Z-Z, Yang M, Zhang Q-X, Xie X-L, Mai Y-W. Micro- and nano-scale deformation behavior of nylon 66-based binary and ternary nanocomposites. Compos Sci Technol 2006;66(16):3097–114.
[23] Vo L, Giannelis E. Compatibilizing poly(vinylidene fluoride)/Nylon-6 blends with nanoclay. Macromolecules 2007;40(23):8271–6.
[24] Bitinis N, Sanz A, Nogales A, Verdejo R, Lopez Manchado M, Ezquerra T. Deformation mechanisms in polylactic acid/natural rubber/organoclay bionanocomposites as revealed by synchrotron X-ray scattering. Soft Matter 2012;8(34):8990–7.
[25] Sweers K, van der Werf K, Bennink M, Subramaniam V. Nanomechanical properties of alpha-synuclein amyloid fibrils: a comparative study by nanoindentation, harmonic force microscopy, and Peakforce QNM. Nanoscale Res Lett 2011;6(1):270.
[26] Zhao B, Song Y, Wang S, Dai B, Zhang L, Dong Y, et al. Mechanical mapping of nanobubbles by peakforce atomic force microscopy. Soft Matter 2013;9(37):8837–43.
[27] Derjaguin BV, Muller VM, Toporov YP. Effect of contact deformations on the adhesion of particles. J Colloid Interf Sci 1975;53(2):314–26.
[28] Wright-Charlesworth DD, Miller DM, Miskioglu I, King JA. Nanoindentation of injection molded PLA and self-reinforced composite PLA after in vitro conditioning for three months. J Biomed Mater Res Part A 2005;74A(3):388–96.
[29] Pillin I, Montrelay N, Bourmaud A, Grohens Y. Effect of thermo-mechanical cycles on the physico-chemical properties of poly(lactic acid). Polym Degrad Stab 2008;93(2):321–8.
[30] Guild FJ, Young RJ, Lovell PA. The influence of material properties on the predicted behaviour of rubber-toughened polymers. J Mater Sci Lett 1994;13(1):10–4.
[31] Bokobza L, Rapoport O. Reinforcement of natural rubber. J Appl Polym Sci 2002;85(11):2301–16.
[32] Mott PH, Dorgan JR, Roland CM. The bulk modulus and Poisson's ratio of "incompressible" materials. J Sound Vib 2008;312(4–5):572–5.
[33] Kummali MM, Miccio LA, Schwartz GA, Alegría A, Colmenero J, Otegui J, et al. Local mechanical and dielectric behavior of the interacting polymer layer in silica nano-particles filled SBR by means of AFM-based methods. Polymer 2013;54(18):4980–6.
[34] Schön P, Dutta S, Shirazi M, Noordermeer J, Julius Vancso G. Quantitative mapping of surface elastic moduli in silica-reinforced rubbers and rubber blends across the length scales by AFM. J Mater Sci 2011;46(10):3507–16.